Energy Advances

ROYAL SOCIETY OF CHEMISTRY

PAPER

View Article Online
View Journal | View Issue

Cite this: *Energy Adv.*, 2024, 3, 1977

van der Waals gap modulation of graphene oxide through mono-Boc ethylenediamine anchoring for superior Li-ion batteries†

Sneha Mandal, [a] Vijayamohanan K. Pillai, *[a] Mano Ranjana Ponraj, [b] Thushara K M, [b] Jebasingh Bhagavathsingh, *[b] Stephan L. Grage, [c] Xihong Peng, [d] Jeon Woong Kang, [e] Dorian Liepmann, [f] Arunachala Nadar Mada Kannan, [g] Velmurugan Thavasi [h] and Venkatesan Renugopalakrishnan[i]

Li-ion batteries stand out among energy storage systems due to their higher energy and power density, cycle life, and high-rate performance. Development of advanced, high-capacity anodes is essential for enhancing their performance, safety, and durability, and recently, two-dimensional materials have garnered extensive attention in this regard due to distinct properties, particularly their ability to modulate van der Waals gap through intercalation. Covalently intercalated Graphene oxide interlayer galleries with mono-Boc-ethylenediamine (GO-EnBoc) was synthesized *via* the ring opening of epoxide, forming an amino alcohol moiety. This creates three coordination sites for Li ion exchange on the graphene oxide nanosheets' surface. Consequently, the interlayer *d*-spacing expands from 8.47 Å to 13.17 Å, as anticipated. When explored as an anode, Li–GO–EnBoc shows a significant enhancement in the stable and reversible capacity of 270 mA h g^{-1} at a current density of 25 mA g^{-1} compared to GO (80 mA h g^{-1}), without compromising the mechanical or chemical stability. Through ^{13}C, ^{7}Li and ^{6}Li MAS NMR, XPS, IR, Raman microscopy, and density functional theory (DFT) calculations, we confirm the positioning of Li^{+} ions at multiple sites of the interlayer gallery, which enhances the electrochemical performance. Our findings suggest that these novel systematically modulated van der Waals gap GO-engineered materials hold promise as efficient anodes for Li-ion batteries.

Received 2nd April 2024,
Accepted 13th June 2024

DOI: 10.1039/d4ya00217b

rsc.li/energy-advances

1. Introduction

The current era is witnessing tremendous technological advances focused on improved energy storage and carbon neutrality for sustainability, as demonstrated by modern and futuristic innovative Li-ion batteries (LIBs). The societal transformation brought by these batteries from being a household item to portable electronics and more recently transportation and grid storage has brought a renaissance in the energy sector. Electric vehicles, from scooters to airplanes, require high performance energy storage, and intermittent energy sources from solar panels and wind farms require high-quality secured storage with maximum energy efficiency and minimum loss.[1–4] Li-ion batteries (LIBs), being one of the most mature battery technologies in the commercial sector, still require better materials in terms of safety, stability, and cost compatibility.[5–7] For example, a low-cost, cobalt-free cathode with excellent performance has recently been reported, and similar innovations abound.[8] The lithium metal anode is considered as one of the most promising candidates for high energy and power density

[a] *Department of Chemistry, Indian Institute of Science Education and Research (IISER), Tirupati, Andhra Pradesh 517507, India. E-mail: vijay@iisertirupati.ac.in*
[b] *Department of Applied Chemistry, Karunya Institute of Technology and Sciences, Coimbatore, Tamil Nadu 641114, India. E-mail: jebasinghb@karunya.edu*
[c] *Karlsruhe Institute of Technology, Institute of Biological Interfaces IBG-2, P.O. Box 3640, 76021 Karlsruhe, Germany*
[d] *College of Integrative Sciences and Arts, Arizona State University, Mesa, AZ 85212, USA*
[e] *Laser Biomedical Research Centre, G. R. Harrison Spectroscopy Laboratory, Massachusetts Institute of Technology, Cambridge, Massachusetts 02139, USA*
[f] *Department of Bioengineering, University of California, 80 Hearst Memorial Mining Bldg., Berkeley, CA 94720, USA*
[g] *The Polytechnic School, Ira A. Fulton Schools of Engineering, Arizona State University, Mesa, AZ 85212, USA*
[h] *Center for Quantum Research and Technology, The University of Oklahoma, 440 W. Brooks Street, Normon, OK 73019, USA*
[i] *Department of Chemistry, Boston Children's Hospital, Harvard Medical School, MGB Center for COVID Innovation, Northeastern University, Boston, MA 02115, USA*

† Electronic supplementary information (ESI) available. See DOI: https://doi.org/10.1039/d4ya00217b

batteries due to its highest theoretical specific capacity (3860 mA h g^{-1}), high voltage, and highest redox potential (−3.04 V *vs.* SHE). Furthermore, the small size of Li^+ ions (76 pm) enables easy intercalation and deintercalation into the host structure during charge/discharge, as well as cyclic stability with excellent coulombic efficiency.[9,10]

The search for better anode materials that are safer and more stable than pure Li metal led to the discovery of several alloy-based composites such as Si–Li and Sn–Li, but these are not suitable for operation in batteries due to their large volume change upon lithiation and subsequent disintegration.[11–13] Of all materials, carbon-based anodes are more promising, primarily because of high reversibility, longer stability, good capacity (372 mA h g^{-1}), excellent capacity retention and low intercalation potential ($\sim$0 V *vs.* Li/Li^+). However, these materials have several limitations, including structural inhomogeneity, inadequate amount of intercalated Li^+ ions, and poor thermal and electrical properties.[14,15] In this context, graphene-based materials have a promising future because of their large surface area (2630 m^2 g^{-1}), electron mobility (15 000 cm^2 V^{-1} s^{-1}), and short diffusion length of Li^+ ($\sim$30 μm) as well as their highly porous structure. Therefore, graphene is considered as an interesting flexible material for superior performance of lithium-ion batteries (LIBs) because in addition to flammability retardation it can enhance the battery capacity, efficiency, energy density, and life cycle.[16–18] Some of the limitations of these materials can also be alleviated by precisely modulating the interlayer *d*-spacing (van der Waals gap engineering), by surface functionalization.[19,20] This also enables the formation of a continuous 2D/3D conducting network formed by graphene, stacked laterally and vertically and thus effectively enhancing the electron and ion transport across the scaffolding, which in principle could improve the rate capability due to faster kinetics at the electrode–electrolyte interface.[21,22] Consequently, graphene oxide (GO) and its surface-engineered variants, with numerous functional groups (*e.g.*, hydroxyl, carboxyl, and epoxy) on their surfaces, especially at the basal planes where organic moieties can be grafted through chemical reactions with the functional groups, have attracted great interest in the development of rechargeable batteries.[23,24] There are several reports on the challenges for the deposition of Li^+ on the surface of graphene and graphite through intercalation.[14,25] For example, Lee *et al.* have achieved Angstrom-level *d*-spacing (7–13 Å) control of graphite oxide using α,ω-diamino organic fillers for high-rate lithium storage.[26] Hyungsub *et al.* have synthesized the Janus nanostructures decorated with Fe_3O_4 nanoparticles and polydopamine on each side of graphene oxide with an interlayer spacing of 14.4 Å for LIBs.[27] Zhao *et al.* have synthesized graphene oxide by grafting the naphthoquinone derivative for ZIBs.[28] Biradar *et al.* have synthesised bio-inspired adenine–benzoquinone–adenine pillar grafted graphene oxide materials with an interlayer spacing of 3.5 Å for supercapacitor application.[29] Gao *et al.* have synthesised stable metal anodes enabled by a labile organic molecule bonded to a reduced graphene oxide aerogel.[30] Banerjee *et al.* have synthesised 1-aza-15-crown-5 functionalized graphene oxide for a 2D graphene-based Li^+-ion conductor.[31] However, some of these materials suffer from sluggish kinetics, and undesirable SEI layer formation, capacity fading and redox changes on Fe can potentially be difficult to control as a parasitic reaction. Moreover, none of the above works shows systematic modulation of the van der Waals gap of GO without reducing it to rGO, by covalent grafting with selective functionalization to a structure-stable material to improve the kinetics, which enables faster mobility of Li-ions during charge/discharge processes.

Here, we report such an unprecedented strategy of intercalation of selectively mono *tert*-butyloxycarbonyl-protected ethylenediamine (EnBoc) in the GO basal planes with the enhancement of interlayer *d*-spacing (13.17 Å) as compared to GO (8.47 Å) without reducing it to rGO. The intercalation of EnBoc on the surface of GO enhances the interlayer spacing due to the covalent conjugation through the ring opening of epoxide by the nucleophilic attack of the primary amine. In the case of lithiation in the enhanced *d*-spacing, it is known that the lithium ions coordinate with the functionalized heteroatoms such as nitrogen and oxygen to form ternary complexes with the intercalant and GO basal planes.[12] By leveraging the intercalation of graphene oxide with appropriate organic molecules such as EnBoc in the design of the electrode, it is possible to covalently cross-link amine functional groups and surface oxide groups on the basal planes of GO to enhance the porous nature, crystallinity, extended conjugation throughout the framework and most importantly being enriched with lithium-ion exchangeable sites that accelerate the intercalation of lithium ions in the pores of the material, and mechanical properties in a more robust manner compared to that of pristine GO. Both our interlayer spacing (13.17 Å) and diffusion coefficient (5.78×10^{-14} cm^2 s^{-1}) values are much better than the values so far obtained, contributing to enhanced performance of these van der Waals-gap engineered electrodes compared to GO. These modified materials are also compatible with Li-battery recycling technology.[32]

2. Materials and methods

2.1 Synthesis of intercalated Li–GO–EnBoc nanosheets

2.1.1 Synthesis of mono-Boc ethylenediamine (EnBoc). The selective EnBoc was prepared according to a previously described method.[33] In brief, 10 molar equivalents of ethylenediamine were placed in 100 mL of dry chloroform in a round bottom flask and cooled to 0 °C. To this mixture, *tert*-butyloxycarbonyl carbonate (CAS #: 24424-99-5, Sigma Aldrich, India) in 70 mL of dry chloroform was added dropwise with constant stirring over a 3 h period. The resulting milky solution was washed with water and then extracted with diethyl ether. During rotary evaporation of the solvent, the unreacted amine was removed and stored under high vacuum to remove the residual solvent. The desired product was isolated as a gummy thick liquid (yield – 82%).

2.1.2 Intercalation of EnBoc on the GO nanosheets: GO–EnBoc. The GO nanosheets were prepared as described

elsewhere.[34] Briefly, EnBoc in tetrahydrofuran (80 mL) was added dropwise over a period of 6 h with constant stirring at 5–8 °C into the dispersed GO sheets (1 g) in 100 mL of double distilled water. The stirring was continued at room temperature for 3 days. A clear colour change from brown to black was observed. The residue was washed with ethanol, acetone and diethyl ether to isolate it as a free-flowing black solid (yield: 850 mg).

2.1.3 Preparation of Li–GO–EnBoc nanosheets. Lithium-ion intercalation was performed by dispersing GO–EnBoc nanosheets in 100 mL of ethylene carbonate (CAS #: 96-49-1, Sigma Aldrich, India) followed by ultrasonication for 30 m and then cooling to 0 °C. $LiClO_4$ (1 g) in 70 mL of ethylene carbonate was added to this solution over a period of 3 h. The reaction mixture was stirred at room temperature for 36 h and the resulting black solid was centrifuged and washed with methanol, acetone, and diethyl ether and stored (yield: 650 mg, 68%) (Fig. 1).

2.2 Material characterisation

Raman spectra were obtained using a custom-built NIR Raman microscope with inverted geometry by placing samples on top of quartz coverslips with a 15 mW, 785 nm excitation laser and integrating the generated signal for 2 m. SEM images were taken using a Carl Zeiss Supra 25 FESEM. FTIR analysis of the GO-based active material was carried out in the spectral range of 450 to 4000 cm^{-1} using the PerkinElmer ATR C117460 instrument. Powder X-ray diffraction of the samples was recorded on a Smart Lab 9 Kw-Rigaku with a monochromatic Cu Kα source (λ = 1.5406 Å) at 45 kV and 200 mA. X-ray photoemission spectroscopy (XPS) measurements were performed on an XPS instrument (Carl Zeiss) using ultra-high vacuum with Al Kα excitation at 250 W. A high-resolution transmission electron microscope (HRTEM; JEOL JEM 2100) was used with a lattice resolution of 0.14 nm and a point-to-point resolution of 0.19 nm operating at 200 kV acceleration voltage and equipped with a Gatan Orius 2k × 2k CCD camera for image recording/processing. Atomic force microscopy (AFM) analysis was performed using a Cypher AFM instrument (Asylum Research, Santa Barbara, CA) and a standard AC-160 tapping mode tip to image the topography of graphene oxide (GO) material. The graphene oxide sheets were prepared by applying the GO powder onto blue tape and transferring it to a Si/SiO_2 substrate using the exfoliation method. The height images were masked and flattened using instrument software. Solid-state NMR spectra were recorded with a 500 MHz Bruker Advance III HD wide-bore spectrometer. For ^{13}C-NMR, the samples were loaded into a 3.2 mm rotor closed with a vessel cap, and measured with a triple-tuned HCN MAS probe under a magic angle spinning (MAS) of 20 kHz. The signal was acquired for 40 ms under 50 kHz ^{1}H decoupling, after an initial 30° pulse of 1.33 μs. Approximately 10 000 scans separated by a recycle delay of 5 s were accumulated. ^{6}Li and ^{7}Li NMR spectral measurements were performed on samples loaded into a 2.5 mm rotor, which was spun at 25 kHz in a double-tuned HX MAS probe. ^{6}Li NMR spectra were acquired for 65 ms after a 1 μs pulse, accumulating 200 000 scans separated by 3 s recycle delay. ^{7}Li NMR spectra were acquired for 80 ms after a 2 μs pulse, accumulating 10 000 scans separated by a recycle delay of 0.3 s. A rotational echo double resonance (REDOR) experiment was performed to measure ^{7}Li to ^{1}H proximities. For this experiment, a series of ^{7}Li NMR spectra were acquired using the above 2.5 mm HX MAS probe, where the acquisition was preceded by a sequence of rotor synchronized 180° pulses of 6.4 μs on the ^{1}H channel to cause recoupling of the ^{7}Li–^{1}H dipolar coupling. The pulses were separated by half rotation periods, and the central pulse was replaced by a 180° pulse on the ^{7}Li channel. The length of the recoupling period was varied to obtain a REDOR curve. This curve was compared to theoretical curves, calculated using self-written software, to obtain a distance estimate.

2.3 Electrochemical measurements

A composite electrode was fabricated from 50% of Li–GO–EnBoc, 20% conductive additive (acetylene black), and 30% binder (teflonized acetylene black, TAB-2) with ethanol using a

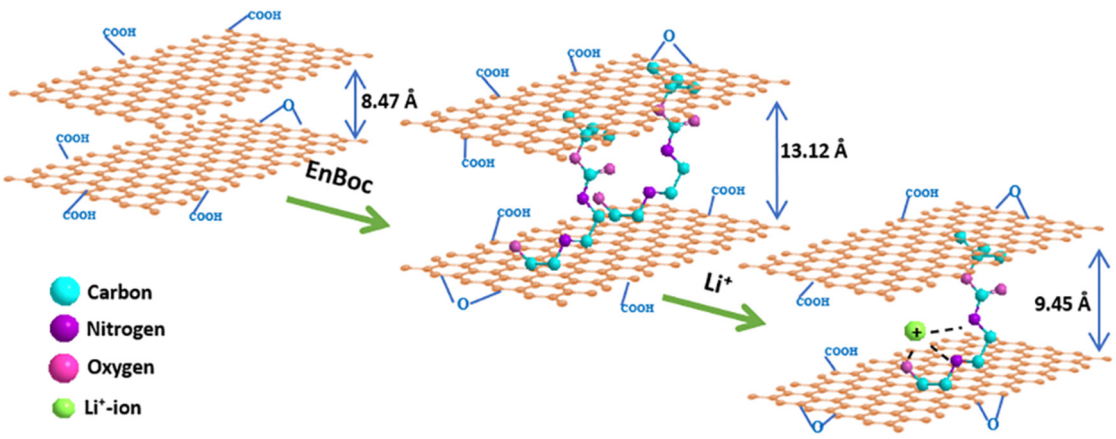

Fig. 1 Schematic illustration (not to scale) of the synthetic methodology to indicate the change in length scales after the anchoring of EnBoc in between the GO basal planes and subsequent intercalation of Li^+ ions.

mortar and pestle (Fig. S1, ESI†). The GO–EnBoc electrode was also prepared in the same manner as Li–GO–EnBoc. A thin film (2.7 μm) of the electrode was pressed onto a 200 mm^2 stainless steel mesh (Goodfellow, UK), which acted as a current collector. The GO electrode was fabricated by the slurry coating method using a doctor blade. In a typical procedure, 90% GO was mixed with 10% binder (polyvinylidene fluoride) to obtain a homogeneous slurry by stirring overnight. Subsequently it was coated on a pre-treated Cu-foil with a doctor blade, and the coated foil was dried in a hot air oven and then pressed under a hot roll press (Tester Sangyo, Japan). Disc electrodes of 12 mm diameter were punched out with the help of an electrode cutter. The active material loading in Li–GO–EnBoc is 3.25 mg cm^{-2} while for GO it is ~1.32 mg cm^{-2}. The as-prepared electrodes were dried in a vacuum oven at 75 °C overnight, prior to cell assembly in an Ar-filled glovebox. The CR2016 cells were made with glass microfiber separators (Whatman, cat. no. 1825-047, UK) using 1 M $LiPF_6$ in ethylene carbonate (EC) : dimethyl carbonate (DMC) (1 : 1 v/v) as the electrolyte (Tomiyama, Japan). Battery tester BCS 805 (Biologic, France) was used for galvanostatic charge/discharge and cyclic voltametric studies of Li–GO–EnBoc, GO–EnBoc and GO electrodes. Electrochemical impedance studies were performed for the electrodes at an open circuit voltage using an AC amplitude of 5 mV (RMS value) in the range of 1 MHz–0.1 Hz using Solartron 1470E electrochemical workstation.

3. Results and discussion

The quality and the degree of functionalization of GO nanosheets were determined by X-ray diffraction (XRD), Fourier transform infrared spectroscopy (FT-IR), X-ray photoelectron spectroscopy (XPS), Raman spectroscopy and solid-state ^{13}C-MAS-nuclear magnetic resonance (SS-NMR). The difference in the inter-layer spacing of GO nanosheets with the covalent anchoring of GO–EnBoc with and without Li-ions was confirmed by XRD analysis. The chemical functionalization with heteroatoms on the basal planes of GO nanosheets often results in the formation of reduced oxygen content in the basal planes, referred to as reduced graphene oxide (rGO), with a corresponding peak at $2\theta \sim 26^\circ$. Accordingly, Fig. 2(a) and Fig. S2 (ESI†) reveal a sharp peak (001) with an enhanced *d*-spacing from 8.71 Å to 13.17 Å for GO and GO–EnBoc respectively, as a result of the intercalation of mono Boc protected amines on the GO basal plane. More interestingly, this *d*-spacing due to the chemical functionalization of the GO basal plane decreases (9.35 Å) after Li-ion insertion (Fig. 2a). The decrease in intensity for GO–EnBoc perhaps arises due to the variation in the crystallite size and the conformational change of the EnBoc molecule on the GO basal plane or because of multiple types of adsorbed lithium due to different relaxation time or due to the low amounts of anchored molecules, as discussed in the NMR section and Fig. S2 (ESI†).

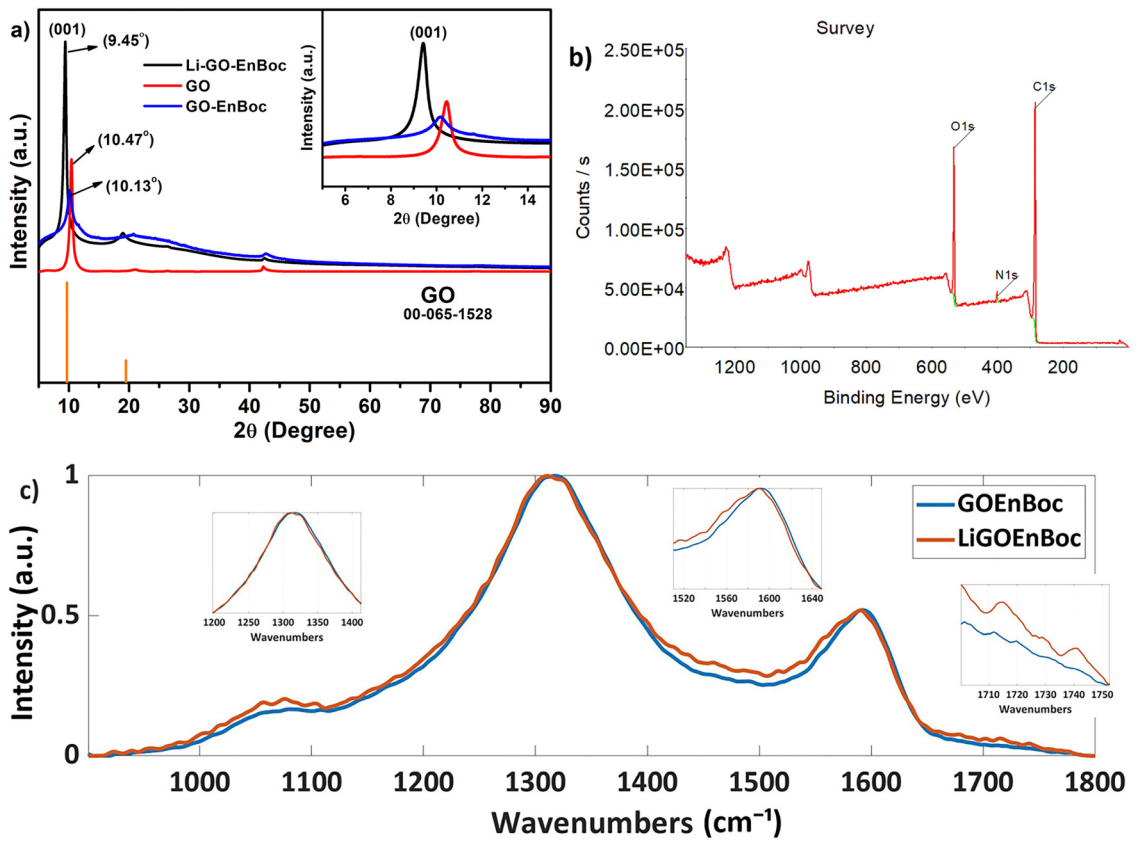

Fig. 2 Comparison of the (a) powder X-ray diffraction (XRD) profile of GO, GO–EnBoc, and Li–GO–EnBoc, (b) XPS survey profile of GO–EnBoc and (c) Raman spectra of GO–EnBoc and Li–GO–EnBoc.

In addition, detailed structural changes and surface properties are elucidated by FT-IR, XPS and Raman analysis. The modifications of the functional group upon intercalation are analysed by FT-IR (Fig. S3, ESI†). The formation of amino alcohol moieties is confirmed by the presence of a broad peak at $\sim$3300 cm^{-1}. The peak at $\sim$1620 cm^{-1} corresponds to the stretching vibrations of C=O groups. Li–GO–EnBoc shows various IR peaks due to the insertion of lithium ions on the basal planes and the coordination moieties. The major functional groups on the graphene nanosheets such as C–N, C–O stretching, C–H bending, appear at 1240, 1155, 1045 cm^{-1} and 1464 cm^{-1}, respectively, for Li–GO–EnBoc and GO–EnBoc.

The chemical nature and the binding energies of the elements present on the surface of GO–EnBoc were investigated by XPS analysis (Fig. 2b). For example, a typical survey spectrum of GO–EnBoc shows a significant peak at 399.8 eV corresponding to the N 1s binding energy confirming the covalent functionalization on the GO surface. The de-convolution of C 1s and N 1s in the high-resolution spectra shows that different carbon and nitrogen components are present in the functionalized GO surface. The C 1s XP spectra of GO–EnBoc (Fig. S4a, ESI†) can be deconvoluted into three components. The peaks centred at 284.4 eV are typically attributed to the C–C bond of the graphitic network, while the peak at 286.5 eV is from the C–N bond. The highest binding energy peak at 287 eV is assigned to the presence of C=O in the terminal carboxyl groups. The N 1s XP spectral peak (Fig. S4b, ESI†) can be deconvoluted into two components at 399.8 and 401.3 eV attributed to amine and imide groups respectively.[35] The atomic fractions of the elements of GO–EnBoc are C – 73.78%, N – 4.79% and O – 21.42%. Structural changes relevant to surface defects occurring during the covalent grafting process from pristine GO to GO–EnBoc and to Li–GO–EnBoc can be analysed by Raman spectroscopy (Fig. 2(c)). Interestingly, the spectra display two characteristic peaks, G band ($\sim$1590 cm^{-1}) and D band ($\sim$1325 cm^{-1}), which correspond to the first-order scattering of the E_{2g} mode and the disordered structures, respectively.[36] The G and D bands have broadened and there is also an increase in the D/G ratio ($I_D/I_G \sim 2$), suggesting that extensive oxidation has induced a significant reduction in the average size of the in-plane sp^2 domains.[37] There is an additional broad peak at $\sim$1050 cm^{-1}, which corresponds to the D* band, for both GO–EnBoc and Li–GO–EnBoc, which reveals the oxygen content in the GO nanosheets.[38] Two additional peaks at $\sim$1715 and 1742 cm^{-1}, for Li–GO–EnBoc, can be seen, indicating the intercalation of Li$^+$ ions in the GO nanosheets.[39]

To characterize the Li-inserted GO–EnBoc sample, we performed solid-state NMR experiments under a magic angle spinning speed of 20–25 kHz. ^{13}C NMR spectra were acquired for Li–GO–EnBoc (Fig. 3a), as well as for the precursor materials GO–EnBoc (Fig. 3b) and GO (Fig. 3c). The three materials show similar signals and differ mainly in the intensity of the individual peaks. The dominant signal at 125 ppm can be assigned to the graphene network.[40] The second largest signal in the Li–GO–EnBoc spectrum (Fig. 3a) at 73 ppm is possibly due to hydroxide modifications in graphene oxide. Similarly, the signal at 62 ppm may represent oxygenated carbon sites such as C–O–C epoxy moieties. In addition, small signals appear at $\sim$45 ppm and $\sim$165 ppm, which can be assigned to aliphatic, quaternary or tertiary carbon atoms and carbonyl moieties, respectively. Comparing the Li–GO–EnBoc spectrum (Fig. 3a) with that of the GO–EnBoc and GO precursor samples (Fig. 3b and c), the spectra agree well in the main signals at 125 ppm and 73 ppm respectively. However, the GO–EnBoc sample (Fig. 3b) exhibits a stronger signal at 62 ppm, which is even larger in the spectrum of GO (Fig. 3c). On the other hand, both

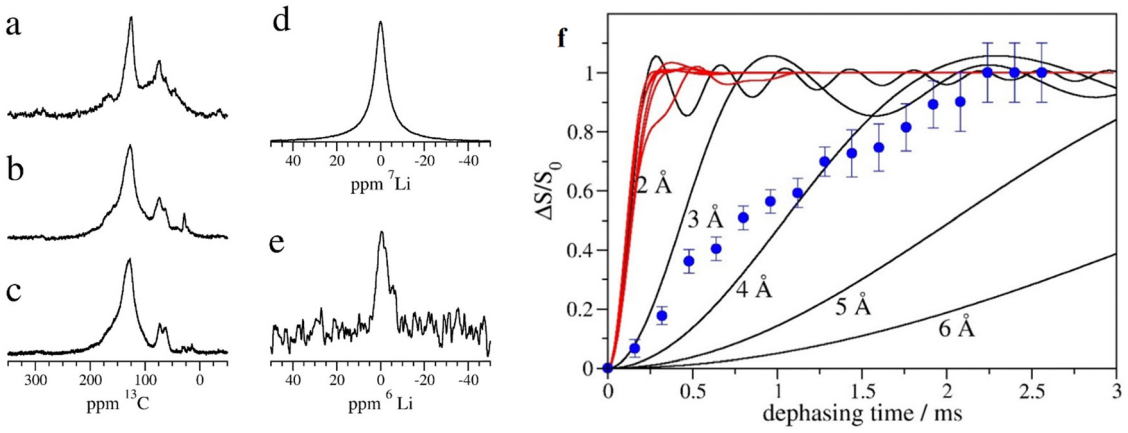

Fig. 3 NMR for Li–GO–EnBoc: (a)–(c) ^{13}C, (d) ^{7}Li, and (e) ^{6}Li. For comparison, the ^{13}C NMR spectra are shown also for the precursors GO–EnBoc (b) and GO (c). The ^{7}Li and ^{6}Li NMR spectra were acquired with a MAS of 25 kHz, and the ^{13}C NMR spectra were acquired with 20 kHz MAS. Short 30° pulses were used for initializing to reduce the effects of saturation. Recycle delays were 0.3 s, 8 s and 5 s in the case of ^{7}Li, ^{6}Li and ^{13}C NMR, respectively. (f) REDOR experiments were performed to elucidate the proximity of Li and hydrogen. ^{7}Li NMR spectra under 25 kHz MAS were acquired after different dephasing periods, during which the ^{7}Li–^{1}H dipolar coupling was reintroduced by RF pulses. The decay curves (blue) are indicative of the distance between the Li atoms and the surrounding hydrogens. Different curves have been calculated for ^{7}Li–^{1}H spin pairs with inter-nuclear distances of 2–6 Å as indicated (black solid lines), to allow an estimate of the Li–hydrogen distance. Theoretical curves have also been calculated for the Li ion and hydrogen coordinates of the DFT models (red solid lines).

GO–EnBoc and GO nearly lack the carbonyl signal at 165 ppm, indicating that during the processing of GO, epoxy-like oxygenated species might be oxidized to carbonyl. A further notable difference is a signal at 28 ppm in the spectrum of GO–EnBoc (Fig. 3b), which is much lower in the spectrum of GO (Fig. 3c) and absent in the Li–GO–EnBoc sample (Fig. 3a). This signal may be attributed to the *t*-butyl moieties of the Boc protection group, which are cleaved off and removed during the acid washing process. It is therefore conceivable that the diamine reacted with the graphene oxide structures during processing and was incorporated covalently into the graphene oxide structure. Some minor signals in the range of 10–30 ppm, which are observed in GO but not in the Li–GO–EnBoc sample, could be small aliphatic modifications in the graphene oxide, which are removed during processing.

The ^{7}Li and ^{6}Li NMR spectra (Fig. 3d and e) of Li–GO–EnBoc show a single, relatively sharp signal near 0 ppm. In addition, a second small signal can be seen at ~ -5 ppm in the ^{6}Li NMR spectrum. This second minor component is absent from the ^{7}Li NMR spectrum, possibly due to a faster T_2 relaxation caused by a larger quadrupole moment in the case of ^{7}Li. The ^{7}Li chemical shift has been correlated to the staging number of the graphene sheets and the Li concentration in intercalated Li graphite compounds.[41–43] A ^{7}Li chemical shift of around 0 ppm, as observed in this study for the major fraction of lithium, has been ascribed to staging numbers larger than 3–4, and to LiC_n compounds with $n \geq 36$. Lower chemical shift values, as observed in the ^{6}Li NMR spectrum for a minor fraction of the sample, have been assigned previously to the solid electrolyte interface layer,[42] and may indicate a small proportion of Li ions outside of graphene-layered structures.

To elucidate the neighbourhood of Li atoms in Li graphene oxide samples, we measured the dipolar couplings between ^{7}Li and ^{1}H using the REDOR (rotational echo double resonance)[44] experiment (Fig. 3f). In this experiment, the averaging effect of the magic angle spinning is partially compensated by a train of radiofrequency pulses affecting one type of nuclei (^{1}H in our case). In this way, the dipolar couplings involving the irradiated nucleus are reintroduced for a certain period (dephasing time), and lead to a reduction of the measured spectrum of an observed nucleus (^{7}Li in our case). The signal reduction has been measured for a number of dephasing times, and is shown in Fig. 3f. A significant reduction in signal is observed, indicating that ^{7}Li is close to ^{1}H. When comparing the experimental curve with curves calculated for ^{7}Li–^{1}H pairs at specific distances (black solid lines in Fig. 3f), the distance of Li to nearby hydrogen atoms would be around 4 Å. As most hydrogen is associated with the graphene oxide layers or with the chemical modifications, we can conclude that the Li atoms are integrated into the graphene oxide structure or near the diamine moieties. In addition, we calculated the REDOR curves which would result from the structures obtained in the DFT simulation (red solid lines in Fig. 3f). The curves look quite similar for all 6 Li ion positions evaluated in the DFT calculations. The experimental results (blue symbols in Fig. 3f) do not agree with the simulated results for the DFT models but would correspond to longer Li–hydrogen distances than in the DFT models. A possible explanation could be that Li^+ occurs in different environments with some Li^+ ions in sites near the diamine modifications, as determined by the DFT calculations, and some at sites further away from hydrogens, *e.g.*, near graphene oxide layers. Such heterogeneity would be compatible with the ^{6}Li spectrum (Fig. 3e), where also 2 signals are observed.

3.1 Morphological and structural characterization

HR-TEM and FE-SEM were used for structural characterization of GO, GO–EnBoc and Li–GO–EnBoc. During the covalent conjugation through the ring opening of epoxide the EnBoc molecules are incorporated between the layers of graphene by the nucleophilic attack of the primary amine. This covalent conjugation between EnBoc and GO results in a wrinkled sheet like morphology, and this stacked architecture of the Li–GO–EnBoc composite can be clearly observed in the scanning electron microscopy (SEM) image (Fig. 4(a) and (b)). For, Li–GO–EnBoc, these sheets are much thinner suggesting that after covalent grafting with EnBoc, the *d*-spacing of GO nanosheets has increased with a higher surface area and interwoven porous 3D network, without disrupting the morphology of GO, which indirectly supports the XRD patterns. In contrast, SEM images of bare GO (Fig. 4a) exhibit a cross-linked porous 3D network with graphene flakes interwoven throughout the structure.[45] The EDX mapping images of GO–EnBoc and Li–GO–EnBoc are shown in Fig. S5 (ESI†), which reveal that oxygen and nitrogen are evenly distributed in the GO nanosheets. Also, from Tables S1 and S2 (ESI†), we observed a significant change in the ratio of atomic weight percentage of carbon to nitrogen from GO–EnBoc (C : N $\sim$ 13 : 1) to Li–GO–EnBoc (C : N $\sim$ 27 : 1) and a slight change in the carbon to oxygen ratio from GO–EnBoc (C : O $\sim$ 4.8 : 1) to Li–GO–EnBoc (C : O $\sim$ 5 : 1), suggesting that the Li-ions are in multiple sites with the functionalised N- and O-atoms of the EnBoc molecule as bolstered by DFT and solid-state NMR results. Fig. 4(f) shows the HR-TEM image of GO–EnBoc revealing a few layers of intercalated GO nanosheets with a sheet-like rippled and crumpled layered morphology which enhanced the interlayer spacing from 8.47 Å to 13.12 Å, whereas drastic wrinkling is visible in the Li–GO–EnBoc (Fig. 4d) nanosheets due to the insertion of Li^+ ions, which interact with the heteroatoms (N, O) of EnBoc with an interlayer spacing of 9.45 Å from 13.12 Å. The similarity of the GO–EnBoc and Li–GO–EnBoc sheet structure suggests that the insertion of Li^+ ions occurs without disrupting the layered morphology of nanosheets. Furthermore, Fig. 4(c) and (e) shows important changes in the stacking sheet structure of GO–EnBoc and Li–GO–EnBoc as evident in the TEM cross-sections where the layers of the GO nanosheets can be discerned clearly. According to these figures, the sheets are parallelly stacked with no major ordering and covalent grafting appears to be uniform. The insets of Fig. 4(d) and (e) show the selected area electron diffraction (SAED) patterns suggesting crystallinity, with no preferred stacking order with the covalent grafting of EnBoc within the GO nanosheets.[46] Fig. S6(a) (ESI†) shows a typical AFM image to give a rough idea on the thickness of the

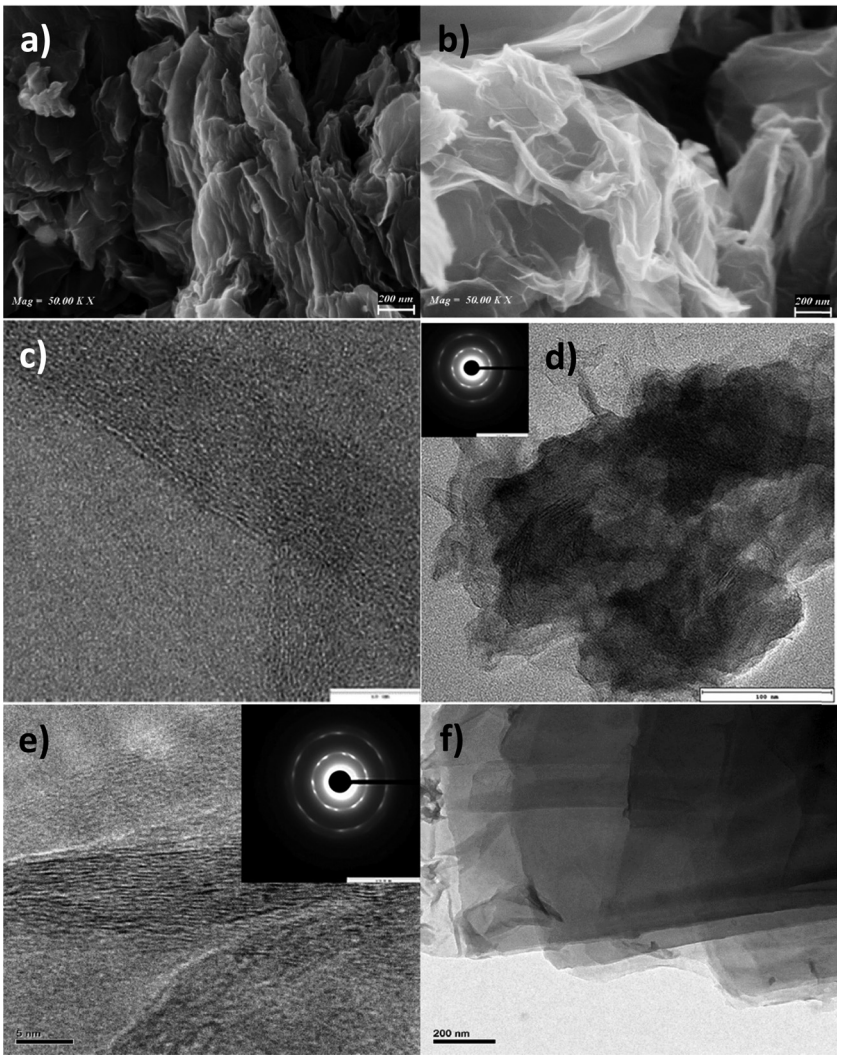

Fig. 4 Field emission-scanning electron microscopic (FE-SEM) images of (a) GO and (b) Li–GO–EnBoc; and high resolution-transmission electron microscopic (HR-TEM) images of (c) and (d) Li–GO–EnBoc and (e) and (f) GO–EnBoc nanosheets (inset: SAED image).

individual sheets. The height profile, Fig. S5(b) and (c) (ESI†), of Li–GO–EnBoc indicates average thickness varying between 2 and 20 nm, which corresponds to about 7–20 layers either due to the stacking of functionalised GO nanosheets or due to the presence of functional groups containing oxygen in the GO created by the oxidation process or due to the anchoring of the EnBoc molecule in the GO basal planes.[47,48]

3.2 Density functional theory (DFT) studies

The first principles DFT[49] calculations were performed using the Vienna *ab initio* simulation (VASP) package[50,51] with the projector-augmented wave (PAW) potentials,[52,53] where Li 1s2s, Na 2p3s, C 2s2p, O 2s2p, N 2s2p, and H 1s electrons are treated as valence electrons. The Perdew–Burke–Ernzerhof (PBE) exchange–correlation functional[54] based on the generalized gradient approximation (GGA) was chosen for general geometry relaxation. The spin-polarized DFT-D3[55] method was adopted for an improved description of van der Waals interaction between layers of GO structures. The wave functions of valence electrons were described using the plane wave basis set with a kinetic energy cut-off of 500.0 eV. The reciprocal space of graphene and graphene oxide models was meshed at 18 × 18 × 1 and 4 × 4 × 1, respectively, using the Monkhorst–Pack method.[56] The energy convergence criterion for electronic iterations is set to be 10^{-5} eV and the force is converged to be less than 0.01 eV $Å^{-1}$ for geometry optimization of the simulation cell.

A graphene model containing 60 carbon atoms with cell dimension 12.34 Å × 12.83 Å was selected to build the defective GO model. The 2D GO model includes one carbon vacancy, 8 OH groups and 3 epoxides with the chemical composition $C_{59}(OH)_8O_3$, which corresponds to 1.67% vacancy density and 20 wt% of oxygen content. The bilayer GO model was created using AB stacking of the fully relaxed single layer GO structure. Intercalant molecule EnBoc was then inserted in between the bilayer GO model. The *z*-vector of the simulation cells was set to be 30 Å to ensure sufficient vacuum space (>14 Å) is included in the calculations to minimize the interaction between the

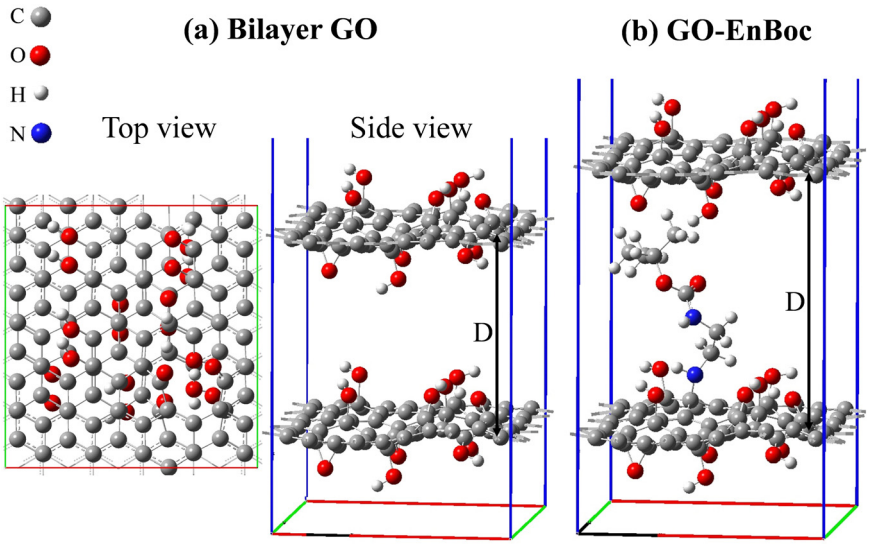

Fig. 5 Snapshots of (a) the bilayer GO model in top and side views, and (b) the bilayer GO with intercalant molecule EnBoc (GO–EnBoc). The red, green and blue cell edges represent *x*, *y* and *z* axes, respectively. The grey, red, white and blue balls denote C, O, H and N atoms, respectively. The interlayer distance of the bilayer GO is labelled as *D*.

system and its replicas resulting from the periodic boundary conditions. After geometry relaxation, the interlayer distance D for the EnBoc intercalant was found to be 13.19 Å (see Fig. 5), which is in excellent agreement with the experimental result of 13.17 Å.

To study the effect of lithiation of the intercalated bilayer GO model, the Li atom was added to 6 different chemical sites in the simulation cell. The binding energy and the interlayer distance D for the geometry relaxed Li–GO–EnBoc systems were calculated and are reported in Table 1. The binding energy was calculated using eqn (1):

$$\mathrm{BE} = E_{\mathrm{system}} - (E_{\mathrm{GO-EnBoc}} + E_{\mathrm{Li}}) \quad (1)$$

where E_{system} is the energy of the lithiated and intercalated Li–GO–EnBoc system, $E_{\mathrm{GO-EnBoc}}$ is the energy of the EnBoc molecule-intercalated GO structure, and E_{Li} is the energy per atom in bulk Li metal. The snapshots of some geometry relaxed Li–GO–EnBoc systems are presented in Fig. 6.

The average equilibrium lithium potentials were calculated according to ref. 57 and 58:

$$V(x) = -\frac{\mu_{\mathrm{Li}}^{\mathrm{cathode}}(x) - \mu_{\mathrm{Li}}^{\mathrm{anode}}}{zF}, \quad (2)$$

$$\Delta G_{\mathrm{r}} = \mathrm{BE}, \quad (3)$$

$$V(x) = -\frac{\Delta G_{\mathrm{r}}}{x}. \quad (4)$$

They reflect the difference in chemical potential between the anode and the cathode. F is Faraday's constant and z is the charge in electrons transported by lithium in the electrolyte. For a half-cell configuration with a Li metal anode and intercalated cathode, $V(x) > 0$ represents the discharge process. The Gibbs free energy change ΔG_{r} can be obtained from the binding energy and the average lithium potential is readily calculated and the results are reported in Table 1.

Among these six sites, the average interlayer distance D is found to be 12.79 Å and the average lithium potential is 2.55 V. The DFT calculation results are in excellent agreement with the experimental results in terms of the intercalation, thereby the enhancement of interlayer spacing. In addition, the calculated average lithium potential of 2.55 V for the Li insertion sites #1–6 agrees well with the experimentally observed cell voltage range 2.0–2.5 V at low capacity as presented in Fig. 7(a). The theoretical specific gravimetric capacity, C_{G} (in mA h g^{-1}), for our models Li–GO–EnBoc with the composition $C_{125}O_{24}H_{31}N_2Li_1$ was determined

Table 1 The calculated binding energy, interlayer distance and average lithium potential of the geometry-relaxed Li–GO–EnBoc systems with Li insertion at six different sites. The case of six Li atoms insertion into the GO–EnBoc system is also listed

System	Binding energy (eV)	Final layer distance D (Å)	Average lithium potential V (V)
Li–GO–EnBoc, Li site 1	−2.08	13.02	2.08
Li–GO–EnBoc, Li site 2	−2.97	13.17	2.97
Li–GO–EnBoc, Li site 3	−2.25	13.24	2.25
Li–GO–EnBoc, Li site 4	−3.37	12.81	3.37
Li–GO–EnBoc, Li site 5	−2.33	13.19	2.33
Li–GO–EnBoc, Li site 6	−2.29	11.30	2.29
Li–GO–EnBoc, 6 Li atoms	−16.14	13.26	2.69

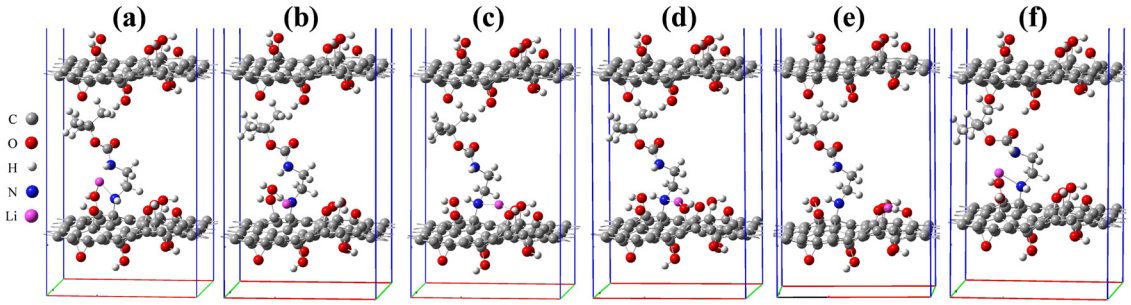

Fig. 6 Snapshots of geometry relaxed Li–GO–EnBoc systems with one Li atom at sites #1–6 (a)–(f), respectively. The red, green and blue cell edges represent *x*, *y* and *z* axes, respectively. The gray, red, white, blue and purple balls represent C, O, H, N and Li atoms, respectively.

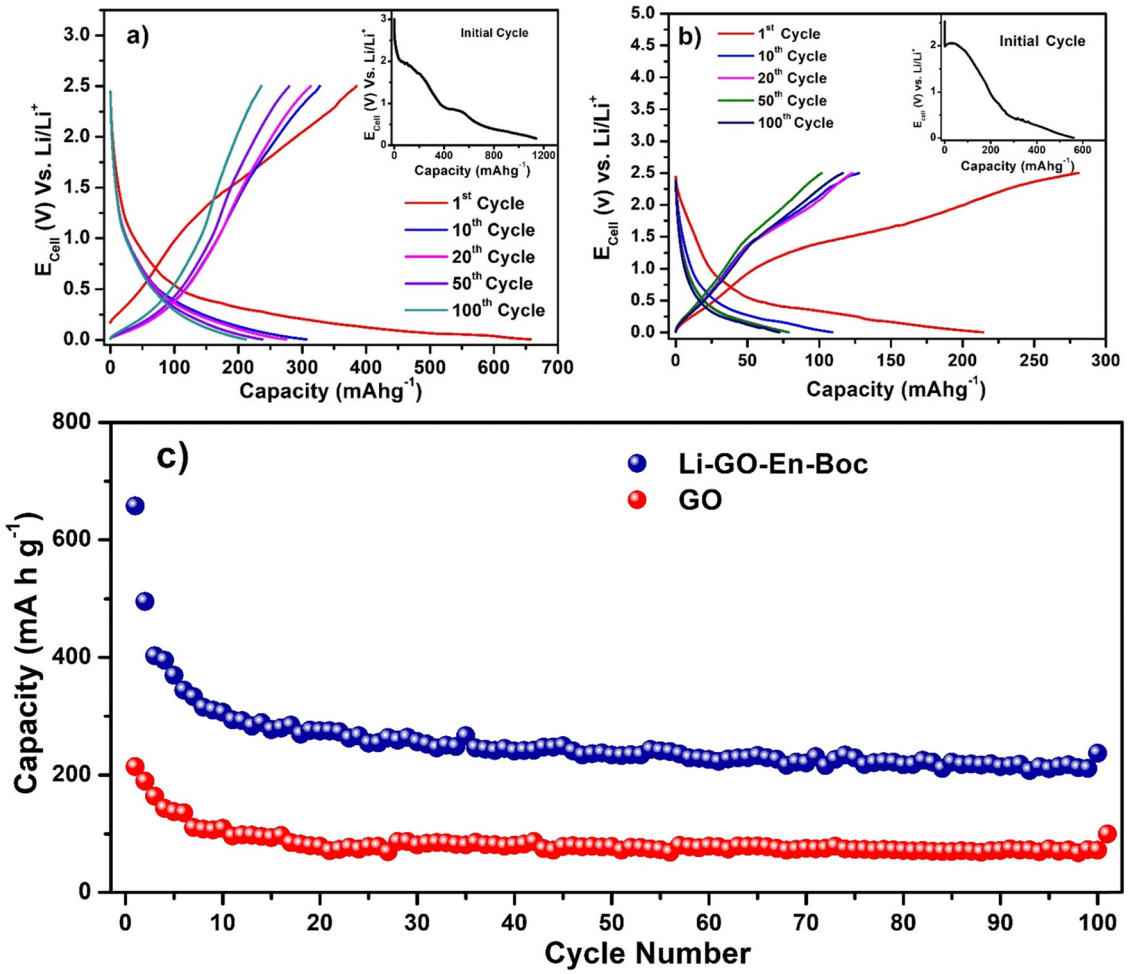

Fig. 7 Charge–discharge profiles for (a) Li–GO–EnBoc and (b) GO electrode cycled at 25 mA g^{-1} between 2.5 and 0.005 V *vs.* Li/Li^+ in 1 M $LiPF_6$ in a 1 : 1 (v/v) mixture of ethylene carbonate (EC) and dimethyl carbonate (DMC) as the electrolyte. (c) Variation in discharge capacity *vs.* cycle number for GO and Li–GO–EnBoc.

to be 13.7 mA h g^{-1} using the equation $C_G = \frac{1000xF}{3600M_W}$, where F is Faraday's constant (9.6485×10^4 C), x is the number of Li inserted, and M_W is the molecular weight of the compound. Multiple Li insertion into the GO–EnBoc system was also considered and calculated with the composition $C_{125}O_{24}H_{31}N_2Li_6$. For the case of a total of 6 Li atoms insertion, the interlayer distance D is 13.26 Å and BE is −16.14 eV, corresponding to an average lithium potential of 2.69 V at a specific gravimetric capacity of 81.0 mA h g^{-1}.

3.3 Electrochemical performance

To evaluate the utility of these materials to reversibly store Li^+ ions and effectively allow charge–discharge performance,

several electrochemical experiments were performed and the open circuit voltage (OCV) was around 3.0–3.2 V for both GO and Li–GO–EnBoc showing that the system is thermodynamically viable.

Fig. 7(a) shows the charge–discharge cycling stability of Li–GO–EnBoc, Fig. 7(b) that of GO and Fig. S7 (ESI†) that of GO–EnBoc electrodes by galvanostatic charge/discharge measurements between 0.005 and 2.5 V *vs.* Li at a rate of 25 mA g^{-1} or 0.06 C similar to what is previously reported.[59–61] Li–GO–EnBoc shows (insets) an initial discharge capacity of 1200 mA h g^{-1}, while GO shows 580 mA h g^{-1} and GO–EnBoc shows 1280 mA h g^{-1}. The initial discharge curve (inset) shows various plateaus at around ~2.02, 0.9, and 0.55 V for Li–GO–EnBoc, around 2.04 and 0.29 V for GO and around ~1.98, 0.97 and 0.53 V for GO–EnBoc, which are attributed to the SEI (solid electrolyte interphase) layer formation on the surface of the electrodes, associated with electrolyte decomposition, formation of Li–organic compounds and irreversible capacity.[62,63] The inset of Li–GO–EnBoc and GO–EnBoc shows various plateaus to indicate that Li-ions are intercalated at various stages, while in GO (inset) these are not very prominent, also there is a straight line of decline in the initial stage because of the conductivity change due to surface functional groups on GO during initial cycles, possibly indicating better charge acceptance. In Fig. 7(b), the first cycle charge capacity of GO is higher than the discharge capacity because Li-ions might get attached to the different functional groups and not all Li-ions are participating in the electrochemical reaction, while in Li–GO–EnBoc, Li-ions are mostly interacting with the amino alcohol moieties. In succeeding cycles, these plateaus disappear, and a smooth curve appears with the first discharge capacity for Li–GO–EnBoc of 680 mA h g^{-1} and a stable reversible capacity of 270 mA h g^{-1}, while GO shows a first discharge capacity of 220 mA h g^{-1} and a stable capacity of 80 mA h g^{-1} after 100 cycles. This is perhaps due to the Li^+ insertion with a stable SEI film, Li^+ binding and a large interlayer spacing of around 13.17 Å with the covalent grafting of the organic molecules in GO as compared to pristine GO with an interlayer spacing of 8.44 Å. Fig. 7(c) shows the variation of discharge capacity with cycling for Li–GO–EnBoc and GO electrodes. Interestingly, these show a stable reversible capacity of 270 mA h g^{-1} and 80 mA h g^{-1} respectively up to 100 cycles. This suggests that the covalent grafting of the organic molecules in GO has resulted in more diffusion of Li-ions and faster dynamics thus enhancing the performance.

Fig. 8(a) shows the cyclic voltammograms (CV) for Li–GO–EnBoc and Fig. 8(b) for GO electrodes and Fig. S8 (ESI†) for GO–EnBoc at a scan rate of 0.1 mV s^{-1}. The CV profiles show reversible lithiation/de-lithiation and the current profile in the first discharge differs from the rest of the cycles as the material undergoes extensive Li-ion re-organisation. This is seen in the form of a broad reduction peak at around ~0.3, 0.6 and 1.5 V *vs.* Li/Li^+ for Li–GO–EnBoc, 0.4, 0.6, 0.83, 1.42 and 2.19 V for GO–EnBoc and about ~0.25, 0.75 and 1.8 V for the GO electrode. Also, during the initial cycle, there is SEI layer formation due to electrolyte decomposition at the electrode surface. In subsequent cycles, the cathodic peak is observed at ~0.9 V for Li–GO–EnBoc, at 0.28 and 0.88 V for GO–EnBoc and at ~0.8, 0.5, and 0.25 V for GO electrodes and anodic peaks at ~0.26 and 1.6 V for Li–GO–EnBoc, at 0.25 and 1.55 V for GO–EnBoc and at ~0.35 V and a broad peak around 1.7 V for GO, showing multiple Li-ion intercalation sites.

Fig. 9(a) shows the Nyquist plot of Li–GO–EnBoc, GO–EnBoc and GO. The impedance measurement is performed by initially applying a high-frequency current and then progressing toward lower frequencies. The responses observed in the high-frequency regime (semi-circle) correspond to charge transfer processes with the lower *x*-axis intercept value giving the solution resistance (R_s) and the higher *x*-axis intercepts giving the sum of solution resistance and the charge transfer resistance (R_{ct}), whereas the responses in the low-frequency regime (tail or nearly linear region) correspond to diffusion-controlled processes.[64,65] Accordingly, Fig. 9(b) shows the Randles plot for Li–GO–EnBoc and GO electrodes which is composed of Z' *versus* $\omega^{-1/2}$, whose slope is equal to the Warburg coefficient (σ) in $\Omega\ s^{-1/2}$. The Warburg coefficient and R_{ct} are then used to

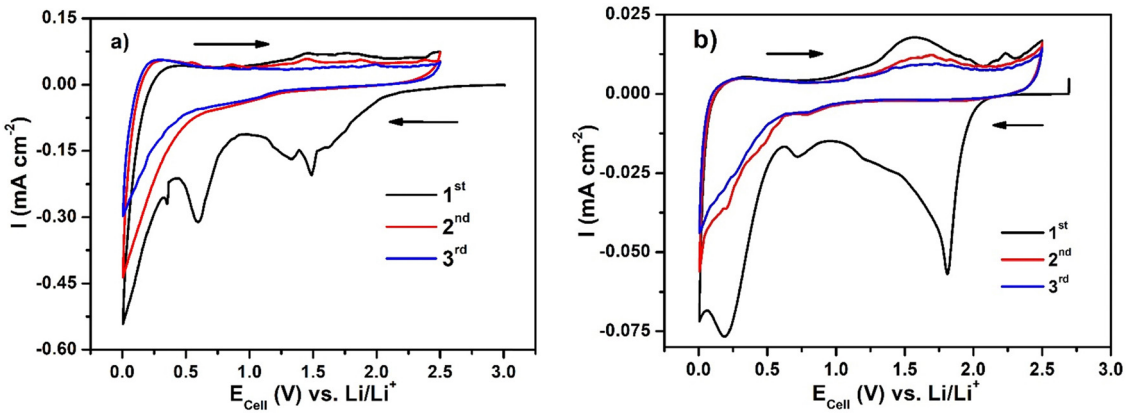

Fig. 8 Cyclic voltammograms of (a) Li–GO–EnBoc and (b) GO electrodes in 1 M $LiPF_6$ in a 1 : 1 (v/v) mixture of ethylene carbonate (EC) and dimethyl carbonate (DMC) as the electrolyte with Li as the counter and reference electrode at a scan rate of 0.1 mV s^{-1}.

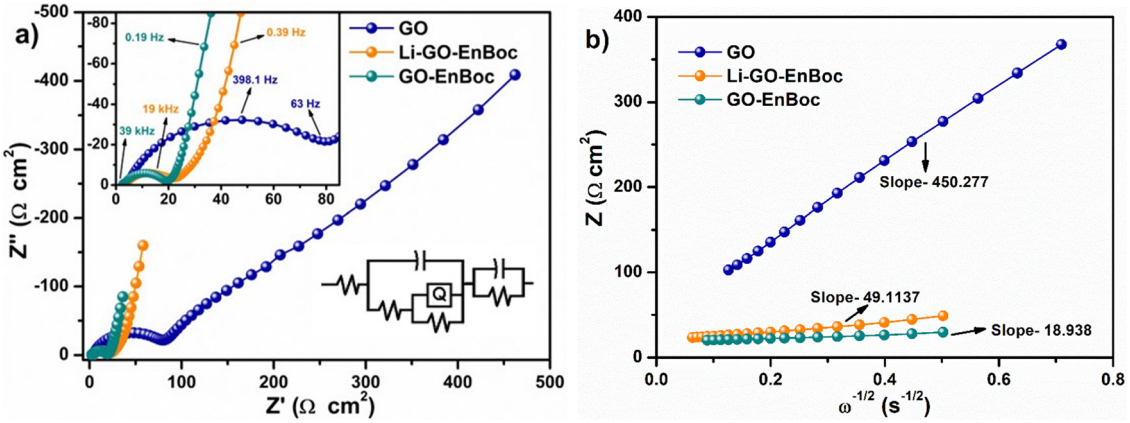

Fig. 9 (a) Nyquist plots for Li–GO–EnBoc, GO–EnBoc and GO and (b) Randles plot for Li–GO–EnBoc, GO–EnBoc and GO.

calculate the diffusion coefficient (D) in $cm^2\ s^{-1}$ and the exchange current density (j_0) respectively using the following equations from the impedance data

$$\sigma = \frac{RT}{n^2F^2A\sqrt{2}}\left(\frac{1}{\sqrt{D}C^*}\right) \quad (5)$$

$$j_0 = \frac{RT}{nFR_{ct}A} \quad (6)$$

where R is the gas constant, T is the temperature in K, n is the number of electrons transferred, F is Faraday's constant, A is the area of the electrode, and C^* is the concentration of the electrode. The results are shown in Table 2.

These results obviously demonstrate that modulation of the van der Waals gap with organic molecules has enhanced the electrochemical performance of the active material. The higher D_{Li^+} (where D is the diffusion coefficient for Li-ions) for Li–GO–EnBoc (twice that on the pristine GO electrode) indicates faster kinetics of the Li^+-ions through the electrolyte channel with the heteroatoms, increasing the rate capability of the electrode.

Various energy storage systems with GO/rGO functionalized anode materials having other electroactive components have been compared and Li–GO–EnBoc (without other electroactive components) displayed quiet comparable performance in terms of capacity and stability as shown in Table 3.

3.4 Post-mortem analysis

Fig. 10(a) and (b) show comparative XRD profiles of the Li–GO–EnBoc and GO electrodes at states of charge (SoC) close to 0 and 1. These are used to study the structural evolution of the material before and after a typical charge–discharge cycle.

Table 2 Comparison of kinetic parameters of Li–GO–EnBoc, GO–EnBoc and pristine GO electrode

Samples	R_s (Ω)	R_{ct} (Ω)	σ (Ω $s^{-1/2}$)	D_{Li^+} ($cm^2\ s^{-1}$)	j_0 (A cm^{-2})
GO	1.8456	95.367	450	6.88×10^{-16}	4.374×10^{-5}
Li–GO–EnBoc	2.75	17.736	50	5.78×10^{-14}	1.28×10^{-3}
GO–EnBoc	2.66	19.09	19	2.076×10^{-13}	8.74×10^{-4}

Table 3 A comparison of the electrochemical performance of Li-ion batteries (LIBs) with carbon anodes

Anode materials	Discharge capacity (mA h g^{-1})	Current density (mA g^{-1})	Potential window (V)	Ref.
Graphene acid	1234	100	0.01–3	66
N-rGO film	529	100	0.01–2.5	67
rGO/FePc	441	50	0.01–3	68
Li–rGO	>1000	25	0.02–3	60
GO–THBQ	1075	50	0.01–3	69
Tp–THzT–CIN/r-GO	123	50	0.01–3	70
rGO@NDC	1400	0.5C	0.01–3	71
P(C-TDPP-AC)/RGO	857	1000	0.01–3	72
AQGO	467	5000	0–3	73
GO	220	25	0.005–2.5	This work
Li–GO–EnBoc	680	25	0.005–2.5	This work

Interestingly, in both the figures, the (001) plane of GO has broadened while the (002) plane has emerged prominently for both SoC-0 and SoC-1. In Fig. 10(a), the d-spacing of the (001) plane (inset) has shifted from 14.09 Å (SoC ~ 0) to 14.35 Å (SoC ~ 1), suggesting volume changes associated with Li incorporation, while in Fig. 10(b), the d-spacing of the (001) plane (inset) has shifted from 13.25 Å (SoC ~ 0) to 13.7 Å (SoC ~ 1) and the difference in interlayer d-spacing during SoC-0 and SoC-1 is 0.45 Å, while for Li–GO–EnBoc, it is 0.26 Å. This suggests that volume changes associated with SoC ~ 0 and 1 have decreased to half with specific functionalisation of GO–EnBoc indicating structure is more robust for Li–GO–EnBoc during lithiation and de-lithiation. This plays an important role in alleviating the stress involved during cycling.

Fig. 11(a) shows that in Li–GO–EnBoc, the Li-ions are more mobile as at both SoC ~ 0 and 1, O–Li peaks are not observed, which are usually found around 500 cm^{-1}, while Fig. 11(b) shows that in GO, the Li-ions are strongly associated with the graphene network, and a sharp peak for the O–Li bond is visible at 484 cm^{-1} at both SoC ~ 0 and 1.[74,75] It is also observed that in both the materials, Li-ions interact with the same kind of environment as most peaks in FT-IR are similar. These results are in excellent agreement with the data obtained from NMR, which is an independent technique.

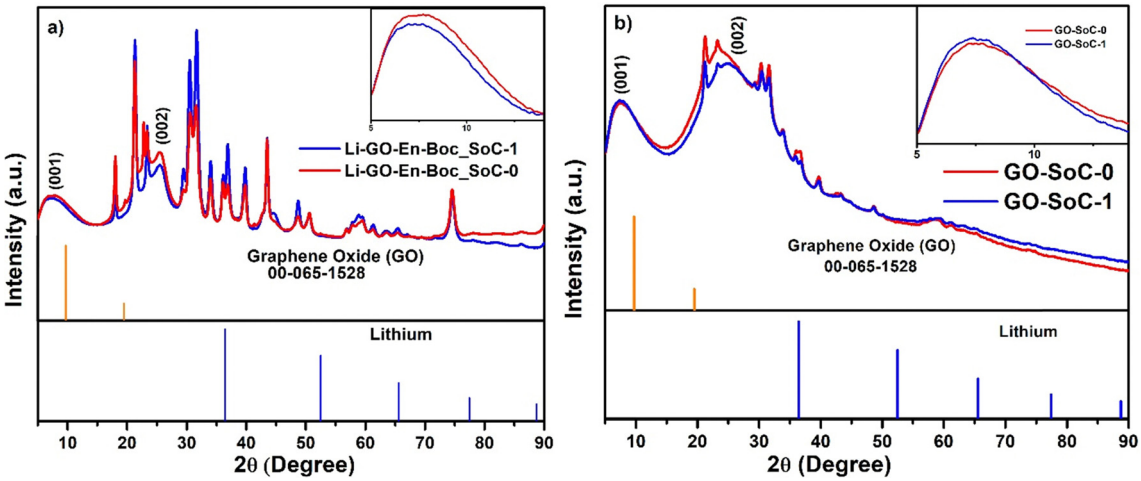

Fig. 10 XRD profiles at state of charge ~0 (after the 1st discharge cycle) and 1 (after the 100th charge cycle) for (a) Li–GO–EnBoc and (b) GO.

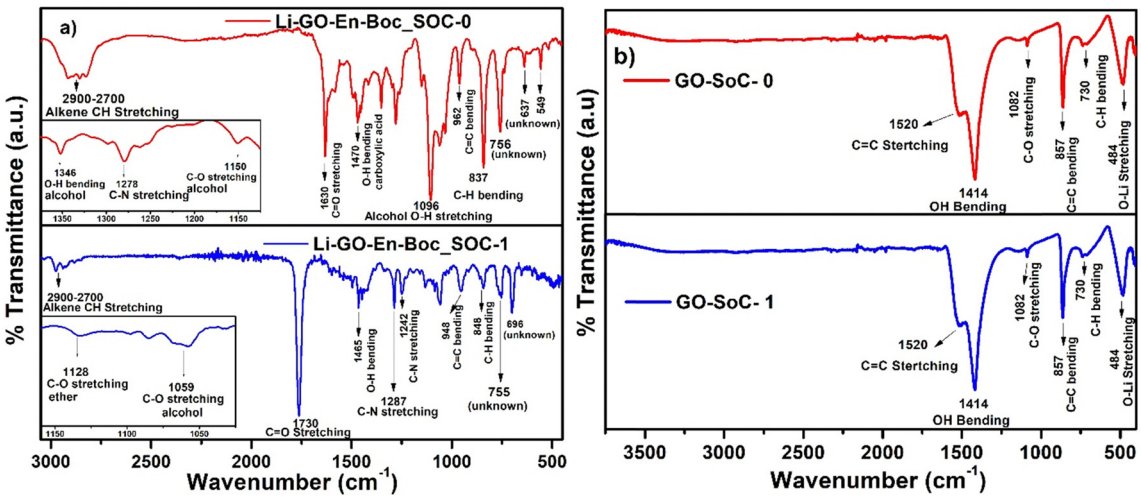

Fig. 11 Comparative FT-IR of (a) Li–GO–EnBoc and (b) GO at states-of-charge (SoC) ~ 0 (after the 1st discharge cycle) and 1 (after the 100th charge cycle).

4. Conclusions

Lithium intercalation continues to play a pivotal role in shaping the applications of currently used Li-ion batteries (LIBs). This study demonstrates that the electrochemical performance and kinetics of graphene-based materials can be enhanced through the modulation of the interlayer gap *via* the covalent anchoring of ethylenediamine through the ring opening of epoxide by the nucleophilic attack of the primary amine. The synthesized Li–GO–EnBoc material exhibits faster Li^+ kinetics owing to a higher Li-ion content and co-ordination with the heteroatoms such as N and O of the EnBoc molecule, thereby improving the electrode's rate capability. Notably, the covalent intercalation of *t*-butyl moiety-bound ethylenediamine on the GO basal planes leads to an enlarged interlayer *d*-spacing (from 8.47 Å to 13.17 Å) without reducing it to rGO, enabling more Li ions to be reversibly accommodated with better mobility. Comprehensive characterization using ^{13}C, ^{7}Li, ^{6}Li-MAS NMR, XPS, IR, Raman, and microscopy confirms the accommodation of Li^+ ions at multiple sites. This, along with an enhanced diffusion coefficient, contributes to an improved capacity value of 270 mA h g^{-1} after 100 cycles with perhaps a negligible fading. The improved electrochemical performance is further corroborated by DFT calculations and solid-state NMR measurements, laying a solid foundation for the potential application of functionalized van der Waals gap GO-engineered materials as efficient anodes for Li-ion batteries.

Author contributions

Sneha Mandal: electrochemical studies, data analysis, manuscript first drafting. Vijayamohanan Pillai: electrochemical studies, drafting and reviewing. Mano Ranjana Ponraj: data

analysis, results validation, drafting. Thushara K. M.: material synthesis and characterization, manuscript drafting. Jebasingh Bhagavathsingh: conceptualization, funding, drafting, reviewing. Stephan L. Grage: ^{13}C, ^{7}Li and ^{6}Li solid state MAS NMR studies. Xihong Peng: density functional theory of intercalated GO. Jeon Woog Kang: Raman studies. Dorian Liepmann: Raman analysis. Arunachala Mada Kannan: electrochemical experimental design, analysis and reviewing. Thavasi Velmurugan: result analysis, draft corrections. Renugopalakrishnan Venkatasan: SEM, AFM, Raman, conceptualizing Li^+ encapsulation in GO and reviewing.

Data availability

Data is available on request from the following authors: Jebasingh Bhagavathsingh (synthesis of materials) – jebasinghb@karunya.edu; Stephan L. Grage (solid-state NMR) – stephan.grage@kit.edu; Xihong Peng (density functional theory) – xihong.peng@asu.edu; Jeon Woog Kang (Raman studies) – jwkang76@mit.edu; Vijayamohanan K. Pillai (electrochemical studies, FT-IR, powder XRD and post-mortem analysis) – vijay@iisertirupati.ac.in; Renugopalakrishnan Venkatasan (SEM and AFM) – v.renugopalakrishnan@northeastern.edu.

Conflicts of interest

The authors are not involved in conflict of interest.

Acknowledgements

The authors sincerely thank the UGC-DAE-Consortium Scientific Research, Kalpakkam Node (no. CSR/Acctts/2016-17/1347) and DST-TDT, DPRP division (no. VI-D&P/562/2016-17/TDT(C)) for their funding to carry out the research. Dr S. L. Grage would like to acknowledge support by the instrument grant INST 121384/58-1 from the Deutsche Forschungsgemeinschaft (DFG) and from the Helmholtz Association (NACIP program). Dr X. H. Peng thanks the Arizona State University Advanced Computing Center for providing computing resources (Agave Cluster). S. M. thanks Dr V. Aravindan for providing the facilities for electrochemical measurements and Akshay Manohar V. for the EDX measurements, Dr Jason Tresback, Center for Nanoscale, School of Engineering and Applied Sciences, SEAS, Harvard University, for AFM images, and Dr Somu Sivasubramanian, Northeastern University, for SEM images and Vijayamohanan would like to thank SERB for the J. C. Bose Fellowship (JCB/2020/000018). Raman studies are partially supported by funds from the National Institutes of Health (Grants to R. P.: R01CA209888 and R21EB022298) and NIH 5P41EB015871.

References

1 M. Armand and J. M. Tarascon, Building better batteries, *Nature*, 2008, **451**, 652–657.
2 C. P. Grey and D. S. Hall, Prospects for lithium-ion batteries and beyond-a 2030 vision, *Nat. Commun.*, 2020, **11**, 6279–6283.
3 S. Liu, L. Kang and S. C. Jun, Challenges and Strategies toward Cathode Materials for Rechargeable Potassium-Ion Batteries, *Adv. Mater.*, 2021, **33**, 2004689.
4 S. Liu, L. Kang, J. Henzie, J. Zhang, J. Ha, M. A. Amin, M. S. A. Hossain, S. C. Jun and Y. Yamauchi, Recent Advances and Perspectives of Battery-Type Anode Materials for Potassium Ion Storage, *ACS Nano*, 2021, **15**, 18931–18973.
5 A. M. Abakumov, S. S. Fedotov and E. V. Antipov, Solid state chemistry for developing better metal-ion batteries, *Nat. Commun.*, 2020, **11**, 4976–4980.
6 A. D. Easley, T. Ma and J. L. Lutkenhaus, Imagining circular beyond lithium-ion batteries., *Joule*, 2022, **6**(8), 1743–1749.
7 A. M. Kannan, V. Renugopalakrishnan, S. Filipek, P. Li, G. F. Audette and L. Munukutla, Bio-Batteries and Bio-Fuel Cells: Leveraging on Electronic Charge Transfer Proteins, *J. Nanosci. Nanotechnol.*, 2009, **9**(3), 1665–1678.
8 R. Essehli, A. Parejiya, N. Muralidharan, C. J. Jafta, R. Amin, M. B. Dixit, Y. Bai, J. Liu and I. Belharouak, Hydrothermal synthesis of Co-free NMA cathodes for high performance Li-ion batteries, *J. Power Sources*, 2022, **545**, 231938.
9 D. Lin, Y. Liu and Y. Cui, Reviving the lithium metal anode for high-energy batteries, *Nat. Nanotechnol.*, 2017, **12**, 194–206.
10 C. K. Chan, X. F. Zhang and Y. Cui, High Capacity Li-ion Battery Anodes Using Ge Nanowires, *Nano Lett.*, 2008, **8**(1), 307–309.
11 H. Wu and Y. Cui., Designing nanostructured Si anodes for high-energy lithium-ion batteries, *Nano Today*, 2012, **7**, 414–429.
12 J. Yin, H. Cao, Z. Zhou, J. Zhang and M. Qu, SnS_2@reduced graphene oxide nanocomposites as anode materials with high capacity for rechargeable lithium-ion batteries, *J. Mater. Chem.*, 2012, **22**, 2396–23970.
13 X. Zhou, L. J. Wan and Y. G. Guo, Binding SnO2 Nanocrystals in Nitrogen-Doped Graphene Sheets as Anode Materials for Lithium-Ion Batteries, *Adv. Mater.*, 2013, **25**, 2152–2157.
14 K. Ji, J. Han and A. Hirata, *et al.*, Lithium intercalation into bilayer graphene, *Nat. Commun.*, 2019, **10**, 275–285.
15 J. Zhang, H. Cao, X. Tang, W. Fan, G. Peng and M. Qu, Graphite/graphene oxide composite as high capacity and binder-free anode material for lithium ion batteries, *J. Power Sources*, 2013, **241**, 619–626.
16 R. Raccichini, A. Varzi and S. Passerini, *et al.*, The role of graphene for electrochemical energy storage, *Nat. Mater.*, 2015, **14**, 271–279.
17 F. Bonaccorso, L. Colombo, G. Yu, M. Stoller, V. Tozzini, A. C. Ferrari, R. S. Ruoff and V. Pellegrini, Graphene, related two-dimensional crystals, and hybrid systems for energy conversion and storage, *Science*, 2015, **347**, 1246501.
18 S. Sharifi-Asl, F. A. Soto, T. Foroozan, M. Asadi, Y. Yuan, R. Deivanayagam, R. Rojaee, B. Song, X. Bi, K. Amine, J. Lu, A. Salehi-khojin, P. B. Balbuena and R. Shahbazian-Yassar,

Anti-Oxygen Leaking $LiCoO_2$, *Adv. Funct. Mater.*, 2019, 1901110.

19 C. J. Sun, M. Sadd, P. Edenborg, H. Grönbeck, P. H. Thiesen, Z. Xia, V. Quintano, R. Qiu, A. Matic and V. Palermo, Real-time imaging of Na^+ reversible intercalation in "Janus" graphene stacks for battery applications, *Sci. Adv.*, 2021, **7**, eabf0812.

20 B. R. Isaac, S. Alwarappan and V. K. Pillai, van der Waals Gap Engineering of Multiwalled Carbon Nanotubes in Ionic Liquids at Room Temperature, *ACS Sustainable Chem. Eng.*, 2023, **11**(46), 16641–16649.

21 J. Zhang, C. Li and Z. Peng, 3D free-standing nitrogen-doped reduced graphene oxide aerogel as anode material for sodium ion batteries with enhanced sodium storage, *Sci. Rep.*, 2017, **7**, 4886–4893.

22 N. Li, Z. Chen, W. Ren, F. Li and H. Ming, Flexible graphene-based lithium-ion batteries with ultrafast charge and discharge rates, *Proc. Natl. Acad. Sci. U. S. A.*, 2012, **109**(43), 17360–17365.

23 E. J. Radich and P. V. Kamat, Origin of Reduced Graphene Oxide Enhancements in Electrochemical Energy Storage, *ACS Catal.*, 2012, **2**, 807–816.

24 S. Stankovich, D. A. Dikin, R. D. Piner, K. A. Kohlhaas, A. Kleinhammes, Y. Jia, Y. Wu, S. T. Nguyen and R. S. Ruof, Synthesis of graphene-based nanosheets via chemical reduction of exfoliated graphite oxide, *Carbon*, 2007, **45**(7), 1558–1565.

25 Y. Sun, J. Tang, K. Zhang, J. Yuan, J. Li, D.-M. Zhu, K. Ozawa and L.-C. Qin, Comparison of reduction products from graphite oxide and graphene oxide for anode applications in lithium-ion batteries and sodium-ion batteries, *Nanoscale*, 2017, **9**, 2585–2595.

26 J. Lee, C. Kim, J. Young Cheong and I.-D. Kim, *et al.*, An angstrom-level *d*-spacing control of graphite oxide using organofillers for high-rate lithium storage, *Chem*, 2022, **8**, 2393–2409.

27 J. Jang, S. H. Song, H. Kim, J. Moon, H. Ahn, K.-Il Jo, J. Bang, H. Kim and J. Koo, Janus Graphene Oxide Sheets with Fe_3O_4 Nanoparticles and Polydopamine as Anodes for Lithium-Ion Batteries, *ACS Appl. Mater. Interfaces*, 2021, **13**, 14786–14795.

28 N. Zhao, P. Song and H. Wen, *et al.*, Graphene oxide grafting naphthoquinone derivative with enhanced specific capacitance and energy density for zinc-ion hybrid supercapacitors, *Ionics*, 2022, **28**, 4425–4433.

29 M. R. Biradar, C. R. K. Rao, S. V. Bhosale and S. V. Bhosale, Bio-inspired adenine-benzoquinone-adenine pillar grafted graphene oxide materials with excellent cycle stability for high energy and power density supercapacitor applications, *J. Energy Storage*, 2023, **58**, 106399.

30 Y. Gao, D. Wang, Y. Kyung Shin, Z. Yan, Z. Han, K. Wanga, M. Jamil Hossain, S. Shen, A. AlZahrani, A. C. T. van Duin, T. E. Mallouk and D. Wang., Stable metal anodes enabled by a labile organic molecule bonded to a reduced graphene oxide aerogel, *Proc. Natl. Acad. Sci. U. S. A.*, 2022, **117**(48), 30135–30141.

31 M. Banerjee, A. Gupta, S. K. Saha and D. Chakravorty, 1-Aza-15-Crown-5 Functionalized Graphene Oxide for 2D Graphene-Based Li^+-ion Conductor, *Small*, 2015, **11**(28), 3451–3457.

32 M. Abdollahifar, S. Doose, H. Cavers and A. Kwade, Graphite Recycling from End-of-Life Lithium-Ion Batteries: Processes and Applications, *Adv. Mater. Technol.*, 2023, **8**, 2200368.

33 T. Vasulinga and A. Ravikumar, Convenient Large Scale Synthesis of N-BOC-Ethylenediamine, *Syn. Commun.*, 2006, 1767–1772, DOI: **10.1080/00397919408010183**.

34 P. Ramesh and B. Jebasingh, Facile and effective oxidation of graphite using sodium metaperiodate, *Mater. Lett.*, 2017, **193**, 305–308, DOI: **10.1016/j.matlet.2017.01.088**.

35 A. Piñeiro-García, S. M. Vega-Díaz, G. Mutton, F. Tristán, D. Meneses-Rodríguez and V. Semetey, Insights in the chemical composition of graphene oxide via a simple and versatile fluorescent labelling method, *ChemNanoMat*, 2021, **7**, 842–850.

36 M. S. Dresselhaus, A. Jorio, M. Hofmann, G. Dresselhaus and R. Saito, Perspectives on Carbon Nanotubes and Graphene Raman Spectroscopy, *Nano Lett.*, 2010, **10**(3), 751–758, DOI: **10.1021/nl904286r**.

37 E. J. Yoo, J. Kim, E. Hosono, H. Zhou, T. Kudo and I. Honma, Large Reversible Li Storage of Graphene Nanosheet Families for Use in Rechargeable Lithium-Ion Batteries, *Nano Lett.*, 2008, **8**(8), 2277–2282.

38 S. Claramunt, A. Varea, D. López-Díaz, M. Mercedes, V. Albert Cornet and A. Cirera, The Importance of Interbands on the Interpretation of the Raman Spectrum of Graphene Oxide, *J. Phys. Chem. C*, 2015, **119**, 10123–10129.

39 E. Pollak, B. Geng, K. J. Jeon, I. T. Lucas, T. J. Richardson, F. Wang and R. Kostecki, The Interaction of Li^+ with Single-Layer and Few-Layer Graphene, *Nano Lett.*, 2010, **10**(9), 3386–3388.

40 A. S. Mazur, M. A. Vovk and P. M. Tolstoy, Solid-state ^{13}C NMR of carbon nanostructures (milled graphite, graphene, carbon nanotubes, nanodiamonds, fullerenes) in 2000-2019: a mini-review, *Fullerenes, Nanotubes Carbon Nanostruct.*, 2020, **28**, 202–213.

41 N. Li and D. Su, In-situ structural characterizations of electrochemical intercalation of graphite compounds, *Carbon Energy*, 2019, **1**, 200–218.

42 K. J. Harris, Z. E. M. Reeve, D. Wang, X. Li, X. Sun and G. R. Goward, Electrochemical changes in lithium-battery electrodes studied using ^7Li NMR and enhanced ^{13}C NMR of graphene and graphitic carbons, *Chem. Mater.*, 2015, **27**, 3299–3305.

43 M. Letellier, F. Chevallier and F. Beguin, In-situ ^7Li NMR during lithium electrochemical insertion into graphite and a carbon/carbon composite, *J. Phys. Chem. Solids*, 2006, **67**, 1228–1232.

44 T. Gullion and J. Schaefer, Rotational-echo double-resonance NMR, *J. Magn. Reson.*, 1989, **81**, 196–200.

45 L. Kang, S. Liu, Q. Zhang, J. Zou, J. Ai, D. Qiao, W. Zhong, Y. Liu, S. C. Jun, Y. Yamauchi and J. Zhang, Tensile Strain-Mediated Spinel Ferrites Enable Superior Oxygen Evolution Activity, *J. Am. Chem. Soc.*, 2023, **145**, 24218–24229.

46 N. R. Wilson, P. A. Pandey, R. Beanland, R. J. Young, I. A. Kinloch, L. Gong, Z. Liu, K. Suenaga, J. P. Rourke,

S. J. York and J. Sloan, Graphene Oxide: Structural Analysis and Application as a Highly Transparent Support for Electron Microscopy, *ACS Nano*, 2009, **3**(9), 2547–2556.
47 S. Stankovich, R. D. Piner, S. B. T. Nguyen and R. S. Ruof, Synthesis and exfoliation of isocyanate-treated graphene oxide nanoplatelets, *Carbon*, 2006, **44**, 3342–3347.
48 P. Szirmai, B. G. Márkus, J. C. Chacón-Torres, P. Eckerlein, K. Edelthalhammer, J. M. Englert, U. Mundloch, A. Hirsch, F. Hauke, B. Náfrádi, L. Forró, C. Kramberger, T. Pichler and F. Simon, Characterizing the maximum number of layers in chemically exfoliated graphene, *Sci. Rep.*, 2019, **9**, 19480.
49 W. Kohn and L. J. Sham, Self-Consistent Equations Including Exchange and Correlation Effects, *Phys. Rev.*, 1965, **144**, A1133.
50 G. Kresse and J. Furthmuller, Efficient iterative schemes for ab initio total-energy calculations using a plane-wave basis set, *Phys. Rev. B: Condens. Matter Mater. Phys.*, 1996, **54**, 11169.
51 G. Kresse and J. Furthmuller, Efficiency of ab-initio total energy calculations for metals and semiconductors using a plane-wave basis set, *Comput. Mater. Sci.*, 1996, **6**, 15.
52 P. E. Blöchl, Projector augmented-wave method, *Phys. Rev. B: Condens. Matter Mater. Phys.*, 1994, **50**, 17953–17979.
53 G. Kresse and D. Joubert, From ultrasoft pseudopotentials to the projector augmented-wave method, *Phys. Rev. B: Condens. Matter Mater. Phys.*, 1999, **59**, 1758.
54 J. P. Perdew, K. Burke and M. Ernzerhof, Generalized Gradient Approximation Made Simple, *Phys. Rev. Lett.*, 1996, **77**, 3865.
55 S. Grimme, J. Antony, S. Ehrlich and H. Krieg, A consistent and accurate ab initio parametrization of density functional dispersion correction (DFT-D) for the 94 elements H-Pu, *J. Chem. Phys.*, 2010, **132**, 154104.
56 H. J. Monkhorst and J. D. Pack, Special points for Brillouin-zone integrations, *Phys. Rev. B: Condens. Matter Mater. Phys.*, 1976, **13**, 5188–5192.
57 M. K. Aydinol and G. Ceder, First-Principles Prediction of Insertion Potentials in Li–Mn Oxides for Secondary Li Batteries, *J. Electrochem. Soc.*, 1997, **144**, 3832–3835.
58 M. K. Aydinol, A. F. Kohan, G. Ceder, K. Cho and J. Joannopoulos, Ab initio study of lithium intercalation in metal oxides and metal dichalcogenides, *Phys. Rev. B: Condens. Matter Mater. Phys.*, 1997, **56**, 1354–1365.
59 Y. Sun, J. Tang, K. Zhang, J. Yuan, J. Li, D. M. Zhu, K. Ozawa and L. C. Qin, Comparison of reduction products from graphite oxide and graphene oxide for anode applications in lithium-ion batteries and sodium-ion batteries, *Nanoscale*, 2017, **9**, 2585–2595.
60 A. Kumar, A. L. M. Reddy, A. Mukherjee, M. Dubey, X. Zhan, N. Singh, L. Ci, W. E. Billups, J. Nagurny, G. Mital and P. M. Ajayan, Direct Synthesis of Lithium-Intercalated Graphene for Electrochemical Energy Storage Application, *ACS Nano*, 2011, **5**(6), 4345–4349.
61 D. Kornilov, T. R. Penki, A. Cheglakov and D. Aurbach, Li/graphene oxide primary battery system and mechanism, *Battery Energy*, 2022, **1**, 20210002.
62 J. Park, J. Sharma, C. J. Jafta, L. He, H. M. Meyer, III, J. Li, J. K. Keum, N. A. Nguyen and G. Polizos, Reduced Graphene Oxide Aerogels with Functionalization-Mediated Disordered Stacking for Sodium-Ion Batteries, *Batteries*, 2022, **8**, 12.
63 C. Zhao, H. Gao, C. Chen and H. Wu, Reduction of graphene oxide in Li-ion batteries, *J. Mater. Chem. A*, 2015, **3**, 18360–18364.
64 V. Vivier and M. E. Orazem, Impedance Analysis of Electrochemical Systems, *Chem. Rev.*, 2022, **122**, 11131–11168.
65 N. O. Laschuk, E. B. Easton and O. V. Zenkina, Reducing the resistance for the use of electrochemical impedance spectroscopy analysis in materials chemistry, *RSC Adv.*, 2021, **11**, 27925–27936.
66 I. Obraztsov, A. Bakandritsos, V. Šedajová, R. Langer, P. Jakubec, G. Zoppellaro, M. Pykal, V. Presser, M. Otyepka and R. Zbořil, Graphene Acid for Lithium-Ion Batteries---Carboxylation Boosts Storage Capacity in Graphene, *Adv. Energy Mater.*, 2022, **12**, 2103010.
67 T. Ludwig, M. Je, H. Choi, T. Fischer, S. Roitsch, R. Müller, R. S. Mane, K. H. Kim and S. Mathur, Boosting nitrogen-doping and controlling interlayer spacing in pre-reduced graphene oxides, *Nano Energy*, 2020, **78**, 105286.
68 D. He, W. Xue, R. Zhao, W. Hu, A. J. Marsde and M. A. Bissett, Reduced graphene oxide/Fe-phthalocyanine nanosphere cathodes for lithium-ion batteries, *J. Mater. Sci.*, 2018, **53**, 9170–9179.
69 Y. Wang, X. Li, L. Chen, Z. Xiong, J. Feng, L. Zhao, Z. Wang and Y. Zhao, Ultrahigh-capacity tetrahydroxybenzoquinone grafted graphene material as a novel anode for lithium-ion batteries, *Carbon*, 2019, **155**, 445–452.
70 S. Mondal, S. Ruidas, K. K. Halankar, B. P. Mandal, S. Dalapati and A. Bhaumik, A metal-free reduced graphene oxide coupled covalent imine network as an anode material for lithium-ion batteries, *Energy Adv.*, 2020, **1**, 697–703.
71 Y. Meng, X. Liu, M. Xiao, Q. Hu, Y. Li, R. Li, X. Ke, G. Ren and F. Zhu, Reduced graphene oxide@nitrogen doped carbon with enhanced electrochemical performance in lithium ion batteries, *Electrochim. Acta*, 2019, **309**, 228–233.
72 Z. Xu, J. Yang, S. Hou, H. Lin, S. Chen, Q. Wang, H. Wei, J. Zhou and S. Zhuo, Thiophene-diketopyrrolopyrrole-based polymer derivatives/reduced graphene oxide composite materials as organic anode materials for lithium-ion batteries, *Chem. Eng. J.*, 2022, **438**, 135540.
73 P. Chen, W. Tao, M. Hu, Y. Xu, Z. Zhang, H. Yu, X. Fu and C. Zhang, Boosting lithium storage by facile functionalization of graphene oxide nanosheets via 2-aminoanthraquinone, *Carbon*, 2021, **171**, 104–110.
74 H. S. Cahyadi, W. William, D. Verma, S. K. Kwak and J. Kim, Enhanced Lithium Storage Capacity of a Tetralithium 1,2,4,5-Benzenetetracarboxylate ($Li_4C_{10}H_2O_8$) Salt Through Crystal Structure Transformation, *ACS Appl. Mater. Interfaces*, 2018, **10**, 17183–17194.
75 M. Armand, S. Grugeon and H. Vezin, *et al.*, Conjugated dicarboxylate anodes for Li-ion batteries, *Nat. Mater.*, 2019, **8**, 120–125.